Contents lists available at ScienceDirect

Materials Science & Engineering A
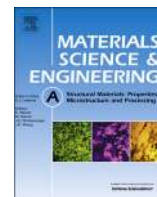
Friction-stir welding of an Al–Mg–Sc–Zr alloy in as-fabricated and work-hardened conditions

S. Malopheyev [a,*], V. Kulitskiy [a], S. Mironov [b], D. Zhemchuzhnikova [a], R. Kaibyshev [a]

[a] Laboratory of Mechanical Properties of Nanoscale Materials and Superalloys, Belgorod State University, Pobeda 85, Belgorod 308015, Russia
[b] Department of Materials Processing, Graduate School of Engineering, Tohoku University, 6-6-02 Aramaki-aza-Aoba, Sendai 980-8579, Japan

ARTICLE INFO

ABSTRACT

The effect of prior work hardening on the microstructure and mechanical properties of a friction-stir welded (FSWed) Al–5.4Mg–0.2Sc–0.1Zr alloy was investigated. The microstructure of the final stir zone was shown to be weakly dependent on the initial condition of the base material; FSW led to the formation of fully recrystallized microstructures with average grain sizes ranging from 1.2 to 1.5 μm and a moderate dislocation density of $\sim 3.5 \pm 1.5 \times 10^{13}$ m^{-2} in the stir zone. The nano-scale Al$_3$(Sc,Zr) dispersoids coarsened from 9 to ~ 15 nm but retained a coherent relationship with the matrix. In contrast, the joint efficiency of the obtained welds was very sensitive to the initial material condition. Nearly full strength joints were obtained in both annealed (O) and partially hardened and stabilized (H323) conditions. However, the joint efficiency was only 65% in the fully hardened condition (H18). The relatively low weld strength for the alloy in the H18 condition was attributed to the elimination of dislocation and substructure strengthening during FSW.

1. Introduction

Al–Mg alloys (5XXX series) are widely used for their good weldability and formability [1]. In the annealed state, these alloys exhibit low-to-moderate yield strengths (YSs) ranging from 90 to 160 MPa for different Mg contents [1,2]. Work hardening can be used to further strengthen these materials to fabricate high-value structural components for critical applications [1,2]. Unfortunately, the work-hardening effect degrades completely during subsequent arc welding, which is the main joining process for these materials [1]. Irrespective of the type of prior working, the weld strength usually does not exceed 85% of the strength of the fully annealed material. The relatively low joint efficiency of the welds is associated with the elimination of the prior work hardening due to the formation of solidification structure in the weld zone. Softening of the heat-affected zones adjacent to the weld zone is attributed to the formation of recrystallized or recovered structures [1]. Al–Mg alloys with these structures exhibit strength as in the annealed condition [1].

High-strength welds in aluminum alloys can be produced using friction-stir welding (FSW) technology [3–5]. FSW is a "solid-state" technique that prevents solidification problems, producing sound joints even in materials that are traditionally considered to be unweldable. In Al–Mg alloys, however, full-strength joints can only be obtained in the annealed state [3–8]. In the hardened state, the weld strength is also relatively low [9,10]. In non-heat-treatable alloys, this effect is mainly related to recrystallization occurring during FSW [3,8,11–12]. In the heat treatable alloys this it is conventionally attributed to the dissolution or coarsening of reinforcement precipitates, e.g., [13].

The material softening under FSW is strongly dependent on the material condition. For instance, the joint efficiency for an AA5083 alloy under fully hardened conditions may drop to 47% [8,9], whereas the weld efficiency of AA5450H116 and AA5052H116 alloys in the partially work-hardened state is 60% or even higher [6,10].

Micro-alloying additions of Sc and Zr can effectively suppress or hinder recrystallization processes in heavily deformed Al–Mg alloys [14–16]. This stabilization of the microstructure can be attributed to the formation of coherent Al$_3$(Sc,Zr) precipitates (i. e., a β'-phase with the L1$_2$ structure) ranging from 7 to 20 nm in size. These dispersoids may also significantly enhance the work hardening effect [17]. Dispersoids generally increase the YS and the ultimate tensile strength (UTS) by more than 50% [14,17–21]. However, conventional fusion welding of Al–Mg–Sc–Zr alloys leads to the dissolution of these unique precipitates and a corresponding

* Corresponding author.
   E-mail addresses: malofeev@bsu.edu.ru (S. Malopheyev),
kulitskiy@bsu.edu.ru (V. Kulitskiy), smironov@material.tohoku.ac.jp (S. Mironov),
zhemchuzhnikova@bsu.edu.ru (D. Zhemchuzhnikova),
rustam_kaibyshev@bsu.edu.ru (R. Kaibyshev).

degradation in the material strength [11,22,23]. Consequently, arc welding cannot increase the joint efficiency beyond 85% in the annealed condition. Thus, hardened products fabricated from these alloys are undesirable as applications to welded structures.

Within this context, FSW is potentially a highly promising technique for joining Al–Mg–Sc–Zr alloys. The peak temperature during FSW of aluminum alloys is believed to remain below ~500 °C [3,24]. This temperature is well below the dissolution temperature of the β'-phase; thus, the $Al_3(Sc,Zr)$ particles are expected to be retained in the welds. However, severe plastic deformation of Al–Mg–Sc alloys at intermediate temperatures can lead to extensive coagulation of the β'-dispersoids and correspondingly degrade their coherency [14,6,25–28]. This behavior can fundamentally degrade the ability of dispersoids to pin dislocations and grain boundaries.

The experimental data on the effect of FSW on $Al_3(Sc,Zr)$ dispersoids are very limited and contradictory. Sauvage et al. have shown that $Al_3(Sc,Zr)$ dispersoids remain unchanged during FSW [12]. In contrast, Vo et al. reported that the average size of the β'-phase increased from 1.5 to ~20 nm along with a loss in the coherency of some of these particles [29]. If a loss in coherency is characteristic of FSW of Al–Mg–Sc alloys, it should not be possible to produce full strength joints in these materials.

To demonstrate the potential of FSW for fabricating full-strength welded structures, the feasibility of this technique for producing high joint efficiency in a novel Al–Mg–Sc–Zr alloy [19] was examined in this study. The primary aim of this work was examining the microstructure–properties relationship. To this end, microstructure and texture evolved in stir zone as well as micro-hardness and tensile properties of the obtained weldments were studied in considerable details.

2. Experimental

Experiments were conducted using an aluminum alloy with a chemical composition of Al–5.4Mg–0.37Mn–0.2Sc–0.09Zr–0.29Ti–0.07Fe–0.04Si (wt%), which was developed in Russia and designated as 1570C Al. This alloy was produced by semi-continuous casting followed by solution treatment at 360 °C for 8 h and subsequent extrusion over a temperature range of 380–320 °C with a 4:1 reduction. This material condition is denoted by O throughout this study. The material was then isothermally rolled either at 300 °C or at ambient temperature parallel to the former extrusion direction for a total rolling reduction of 80%: the two resulting rolled conditions are denoted here as H323 and H18, respectively.

The preprocessed (base) materials were then butt-welded parallel to the deformation (i.e., extrusion or rolling) direction using the FSW technique. The thickness of the welded sheets was 2.4 mm in the O and H18 conditions or 2.0 mm for the H323 material. Other dimensions of the welded plates are shown in Fig. 1. The welding tool was fabricated from tool steel and consisted of a shoulder with a diameter of 12.5 mm and an M5 cylindrical pin, which was 1.9 mm in length. To avoid the formation of a kissing-bond defect, a double-sided FSW was applied in mutually opposite directions, such that the advancing (AS) and retreating sides (RS) reversed from the upper to the bottom surfaces of the welds. The welding process was performed using an AccuStir 1004 FSW machine at a tool rotational speed of 500 rpm and a tool travel speed of 75 mm/min. During FSW, the tool was tilted by 2.5° from the sheet normal such that the rear of the tool was lower than the front. FSW was performed using the position control scheme. The plunge depth of the tool was controlled to be 2.06 mm in the O and H18 conditions and 1.45 mm in the H323 condition. For consistency with the FSW
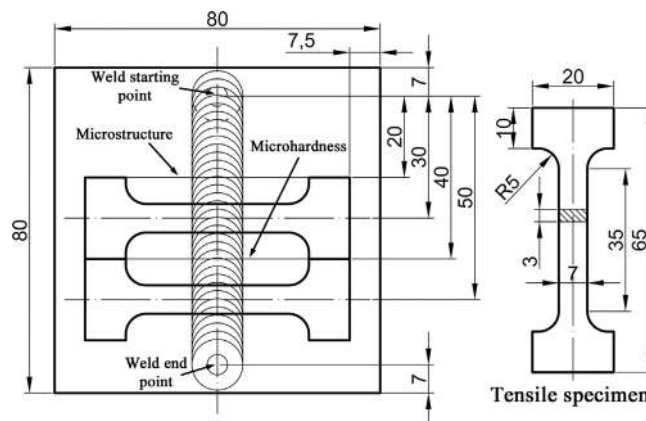

Fig. 1. The weld and specimen dimensions. See Section 2 for details.

literature, the principal directions of the welding geometry are denoted throughout this study as the welding direction (WD), the transversal direction (TD) and the normal direction (ND) of the welded sheets [3–5].

The microstructures in the base and welded materials were examined in the transversal cross-sections of the welds by optical microscopy, electron backscatter diffraction (EBSD) and transmission electron microscopy (TEM). The location of the microstructural observations along the weld path is shown in Fig. 1. The metallographic observations were carried out using an Olympus GX71 optical microscope. The high-resolution EBSD analysis was conducted using a FEI Quanta 600 field-emission-gun scanning electron microscope (FEG-SEM) equipped with TSL OIM™ software. The TEM study was performed using a JEM-2100EX TEM operating at 200 kV. The samples for the metallographic observations were prepared using conventional polishing techniques followed by final etching in Keller's reagent. Suitable surfaces for the EBSD studies and twin jet-polished surfaces for the TEM studies were obtained using electro-polishing in a solution of 25% nitric acid in ethanol.

The examined microstructures exhibited different scale sizes; therefore, an EBSD scan step size ranging from 0.5 μm to 0.15 μm was used. To improve the reliability of the EBSD data, small grains comprising 3 or fewer pixels were automatically removed from the acquired EBSD maps using the grain-dilation option in the TSL software. In addition, a lower-limit boundary-misorientation cut-off of 2° was used to eliminate spurious boundaries caused by orientation noise. In the grain-boundary EBSD maps, the low-angle boundaries (LABs) ($2° < \theta < 15°$) and the high-angle boundaries (HABs) ($\theta \geq 15°$) were depicted as red and black lines, respectively. The sizes of the equiaxed grains were quantified by measuring the grain area and calculating the equivalent grain diameter by modeling each grain as a circle in accordance with the grain reconstruction method [30].

To view the microstructure distribution in the weld zone more broadly, the microhardness profiles were measured across the transversal cross-sections of the welds at the sheet mid-thickness; the location of the microhardness measurements along the weld path is shown in Fig. 1. Vickers microhardness data were obtained by applying a load of 100 g with a dwell time of 15 s in a Wolpert 402MVD microhardness tester.

Room-temperature tension tests to failure were conducted at a constant crosshead velocity corresponding to a nominal strain rate of 10^{-3} s^{-1} in an Instron 300LX universal testing machine. The mechanical properties of the welds were evaluated using transverse tensile tests. The transverse tensile specimens were cut perpendicular to the WD with a gauge section that was 7-mm wide and 35-mm long and included all of the characteristic FSW

microstructural zones at two locations along the weld line, as shown in Fig. 1. The values of strength and ductility were averaged over tests of these two samples at each experimental point. The mechanical properties of the stir zone material were examined using longitudinal tensile tests. The longitudinal tensile specimens were cut along the weld centerline with a gauge section that was 35-mm long and 3-mm wide and included only the stir zone material. The upper and lower surfaces of all of the tensile specimens were mechanically polished to achieve a uniform thickness and to prevent the surface defects from affecting the tensile properties.

3. Results

3.1. Base materials

Fig. 2 shows the selected portions of the grain-boundary EBSD maps and the respective misorientation-angle distributions obtained from the base materials in the O, H323 and H18 conditions. Fig. 3 shows the representative TEM images of the

microstructures of these materials. Table 1 summarizes the relevant material microstructural characteristics.

The grain structure in the O condition primarily consisted of coarse grains $\sim$90-μm long and approximately 30 μm thick, which were elongated in the extrusion direction (see Fig. 2a and Table 1). A minor fraction of relatively fine ($\sim$5 μm) grains was also present along the boundaries of the coarse grains (see the selected area in Fig. 2a). The coarse grains contained a developed subgrain structure and an LAB fraction as high as $\sim$75% (see Fig. 2b and Table 1). The dislocations were typically arranged in well-defined LABs (Fig. 3a) with a low free dislocation density (Table 1).

At high magnifications, homogeneously distributed nano-scale ($\sim$9 nm) precipitates were also seen in the interior of the grains (Fig. 3b). Some of these particles featured a characteristic coffee-bean contrast (encircled in Fig. 3c), reflecting their coherence with the matrix. These dispersoids were interpreted to be $Al_3(Sc,Zr)$ precipitates. The dispersoids were typically associated with the aluminum matrix through the characteristic $\{111\}_{Al}\|\{111\}_{\beta'}$ $\langle100\rangle_{Al}\|$ $\langle100\rangle_{\beta'}$ relationship (see the diffraction pattern in the top right corner of Fig. 3b), which is a signature of coherency. A minor fraction of coarser ($\sim$40 nm in size), round and incoherent Al_6Mn

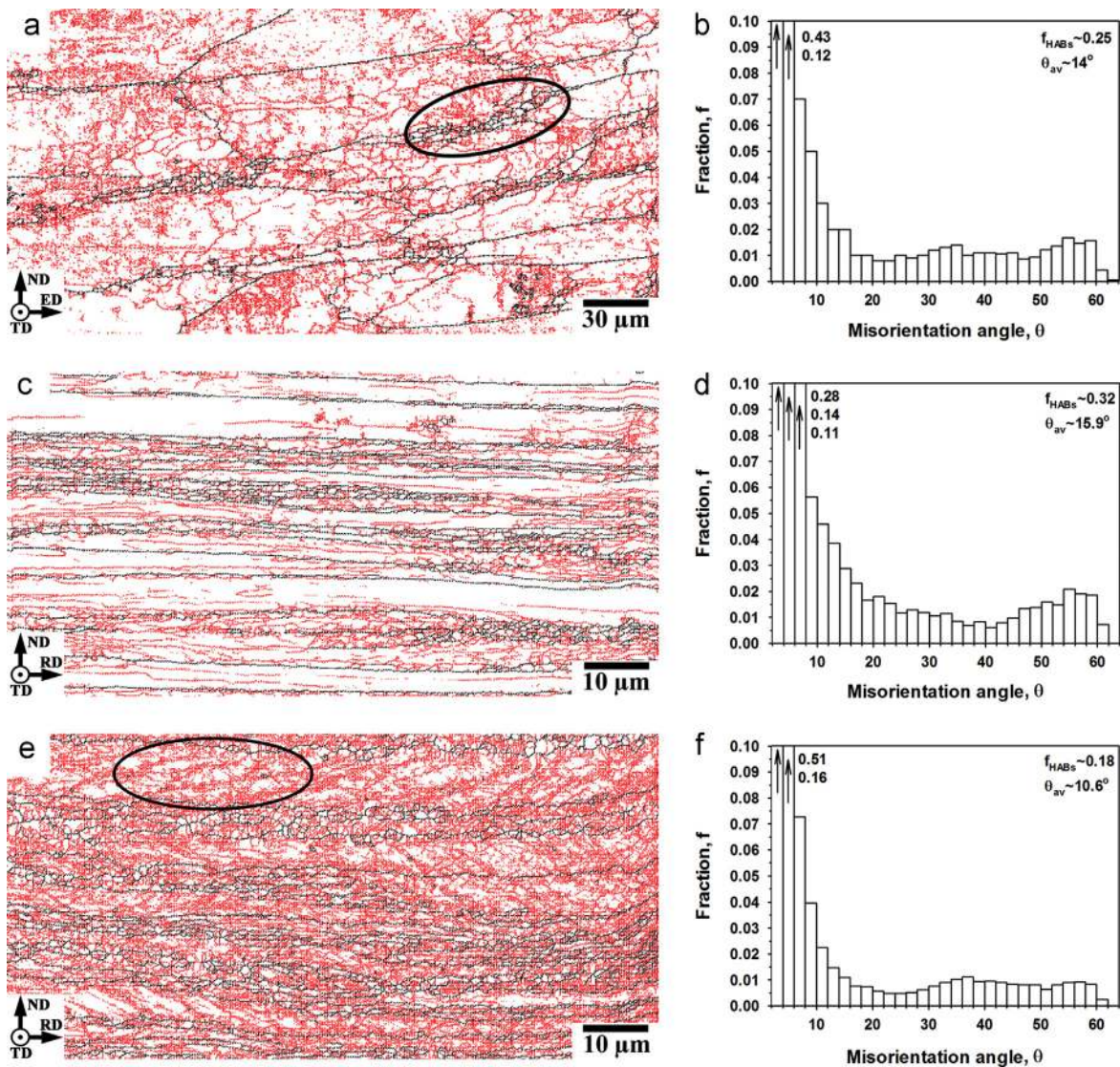**Fig. 2.** Grain-boundary EBSD maps and respective misorientation-angle distributions showing the microstructure of the base material in (a, b) the O condition, (c, d) the H323 condition and (e, f) the H18 condition: LABs and HABs are shown as red and black lines, respectively; ED, TD, RD and ND denote the extrusion, transversal, rolling and normal directions, respectively (note the differences in scale; see Section 3.1 for details).
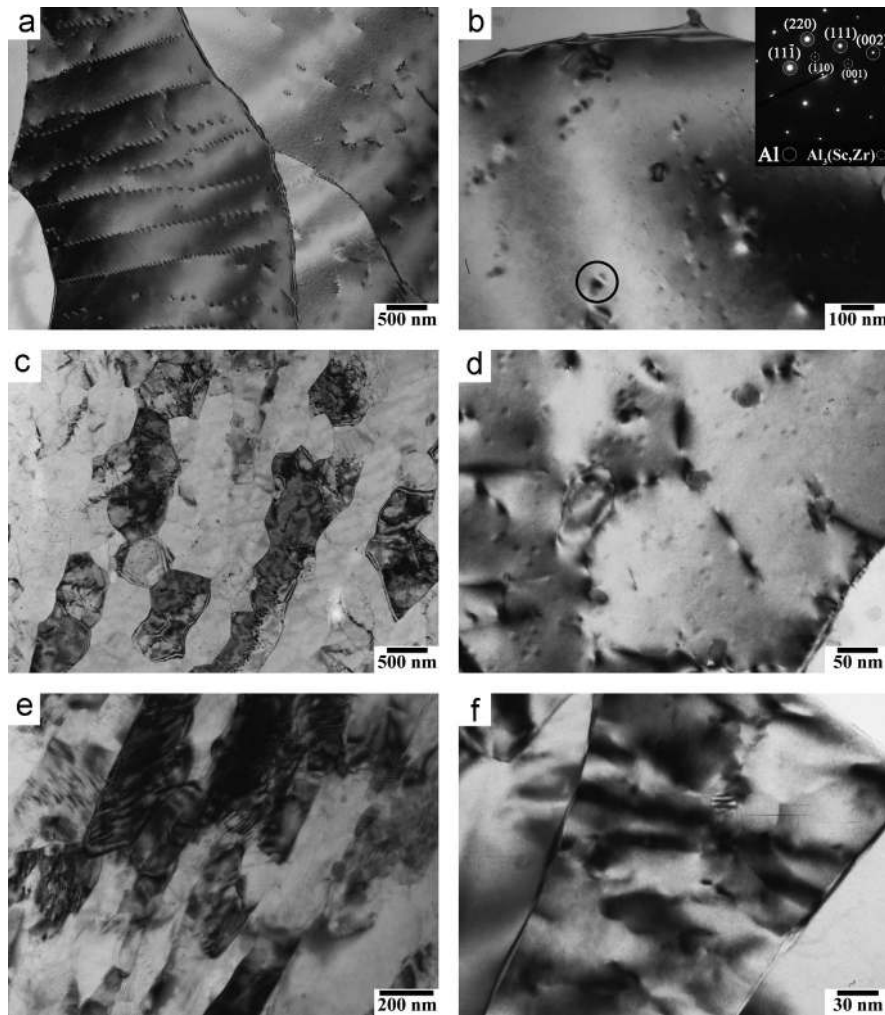
Fig. 3. TEM images of the microstructures of the base material in (a, b) the O condition, (c, d) the H323 condition and (e, f) the H18 condition (note the differences in scale): in (b), the diffraction pattern in the top right corner shows the coherent nature of the $Al_3(Sc,Zr)$ precipitates (see Section 3.1 for details).

Table 1
Microstructural characteristics of base materials.

Material condition	Mean grain thickness (EBSD), μm	Subgrain size (TEM), μm	Dislocation density (TEM), m^{-2}	HAB fraction (EBSD), %
O	30	1.7	10^{13}	25
H323	3.1	0.7	4×10^{13}	32
H18	3.8	0.2	8×10^{14}	18

particles was also found within the interior of the grains (not shown).

Large rolling reductions during either hot or cold rolling produced a thin (~ 3–$4\,\mu m$) ribbon grain structure in both the H323 and H18 conditions (see Fig. 2c and e, respectively). These microstructures presumably originated from the geometrical compression of the coarse grains in the O-material during rolling. The substructures that evolved in the H323 and H18 states were distinctly different from each other.

In the H323 condition, the substructure consisted of nearly equiaxed subgrains with a mean size of $\sim 0.7\,\mu m$ (see Fig. 3c and Table 1). Considering that these subgrains were not clearly visible in the EBSD map (Fig. 2c), the typical sub-boundary misorientation was presumably below the EBSD detection limit (i.e., $2°$). A 68% LAB fraction was measured by EBSD (Table 1). A relatively low density of the free dislocations within the subgrains was measured

at $\sim 4 \times 10^{13}\,m^{-2}$ (Table 1). The precipitation pattern was found to be generally similar to that observed in the hot extruded condition (Fig. 3d).
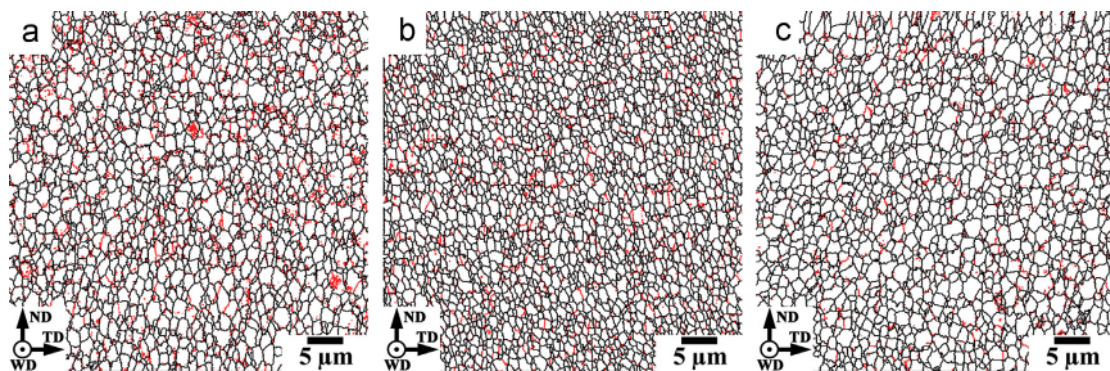
The substructure in the H18 condition was more complex. On a relatively coarse scale, this substructure often comprised two intersecting sets of boundaries inclined to the rolling direction at $\sim 30°$ (encircled in Fig. 2e). On a finer scale, these boundary sets were composed of bands of nearly parallel boundaries with a boundary spacing of $\sim 0.2\,\mu m$ (see Fig. 3e and Table 1). The development of such microstructures is well documented in cold rolled fcc cubic metals [1,32–34] and is conventionally attributed to the activation of the grain subdivision process. The EBSD-detected LAB fraction was 82% (Table 1). A particularly important observation was that the cold rolled material had a high dislocation density of $\sim 8 \times 10^{14}\,m^{-2}$ (Table 1). This result is believed to be associated with the pinning effect of the $Al_3(Sc,Zr)$ precipitates, which prevent rapid rearrangement of the dislocations at ambient temperature. The TEM images showed that the $Al_3(Sc,Zr)$ dispersoids primarily retained their size and, consequently, their coherent nature (not shown).

3.2. Friction-stir welds

Fig. 4 shows low-magnification optical images of transversal cross-sections of friction-stir welds obtained in the O, H323 and H18 conditions. There were no evident volumetric defects in the
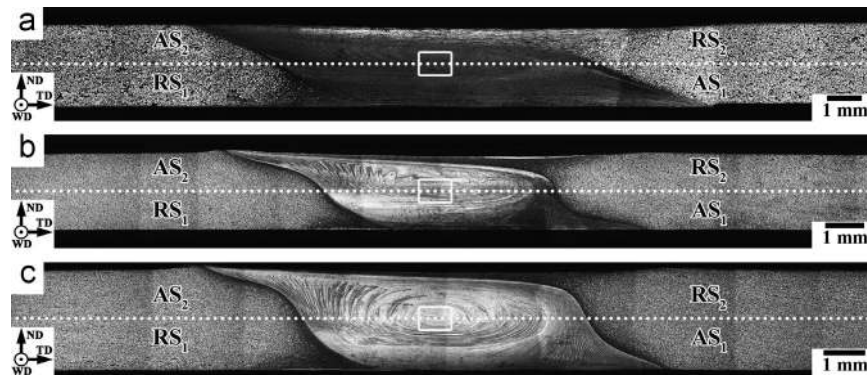
Fig. 4. Low-magnification overviews of transversal cross-sections of friction-stir welds produced in O condition (a), H323 condition (b) and H18 condition (c). WD, TD and ND are welding, transversal and normal directions, respectively. $AS_1(AS_2)$ and $RS_1(RS_2)$ denote advancing and retreating sides at first and second passes, respectively. The areas of EBSD analysis and TEM studies are marked by white squares. The dotted lines indicate microhardness profiles shown in Fig. 10.

Fig. 5. EBSD grain-boundary maps showing the microstructure in the central part of the stir zone in (a) the O condition, (b) the H323 condition and (c) the H18 condition: LABs and HABs are depicted as red and black lines, respectively; WD, TD, and ND denote the welding, transversal, and normal directions, respectively.

welds. This result confirms the feasibility of FSW for producing sound joints in Al–Mg–Sc alloys, as reported in earlier works [9,11,22,23].

A distinct stir zone was evident in each weld. In all of the cases studied, the stir zone was asymmetric relative to the weld centerline and exhibited a characteristic tear-like shape. A similar morphology of the stir zone that evolved during FSW of an Al–Mg–Sc alloy was recently reported in Refs. [11,35].

The stir zone in the O condition was somewhat different from those in the H323 and H18 samples. In the O condition, the optical contrast was very homogeneous (Fig. 4a), whereas clear flow patterns and onion-ring structures [3,13,36] were seen in the rolled materials (Fig. 4b and c). This discrepancy may indicate differences in the material flow between the annealed and hardened conditions during FSW.

3.3. Microstructure and texture in stir zone

3.3.1. Microstructure

Figs. 5 and 6 show the EBSD grain-boundary maps and representative TEM images, respectively, taken from the central parts of the stir zones in the O, H323 and H18 conditions (the location of the microstructural observations is indicated in Fig. 4). Tables 2 and 3 summarize the relevant microstructural characteristics.

The microstructures that evolved in the stir zone for all of the three conditions were generally the same. In all of the cases studied, the microstructure was dominated by low-aspect ratio grains with a mean grain size of ~ 1.5 µm (see Fig. 5 and Table 2). Therefore, a drastic grain refinement occurred during FSW. The grains were typically completely delineated by an HAB perimeter and contained nearly no LABs (Fig. 5). The HAB fraction was as high as 80–90% (Table 2). The grain boundaries in the TEM images

often exhibited a characteristic fringe contrast, indicating that they were strain-free (see Fig. 6a, c and e). The dislocation density was low (Table 2). In general, the microstructure appeared to be completely recrystallized for all of the cases studied. This observation was in agreement with previous studies of friction-stirred Al–Mg–Sc alloys [11,12,23,31,35].

As expected, the nano-scale $Al_3(Sc,Zr)$ precipitates were retained during FSW (see Fig. 6b, d and f). A quantitative analysis showed that the volume fraction of the dispersoids remained unchanged, whereas their mean size increased from 9 nm to 13–16 nm (see Table 3 and Fig. 7). However, this particle size was well below the critical diameter that is considered to degrade the particles' coherency (116 nm) [14]. Indeed, diffraction analysis showed that the orientation of the $Al_3(Sc,Zr)$ dispersoids was related to that of the aluminum matrix through the $\{111\}_{Al}\|\{111\}_{\beta}'$ $\langle100\rangle_{Al}\|\langle100\rangle_{\beta}'$ orientation relationship (see the top right corners of Fig. 6b, d and e). This result confirmed the coherent nature of these precipitates in the stir zone.

3.3.2. Texture

The material flow during FSW is believed to be close to a simple shear deformation mode [37]. The shear direction is expected to be tangential to the tool surface; specifically, the shear direction should be nearly parallel to the TD in the stir zone center [37]. In general, the shear plane orientation is not clear. Depending on the nature of the welded material, the tool design and the FSW parameters, the shear plane orientation may be close to either the tool column surface or the shoulder surface [37]. The development of a specific elliptically shaped stir zone and the formation of an onion-ring structure in the H323 and H18 welds (see Fig. 4b and c) suggest that the material flow in these cases was primarily driven
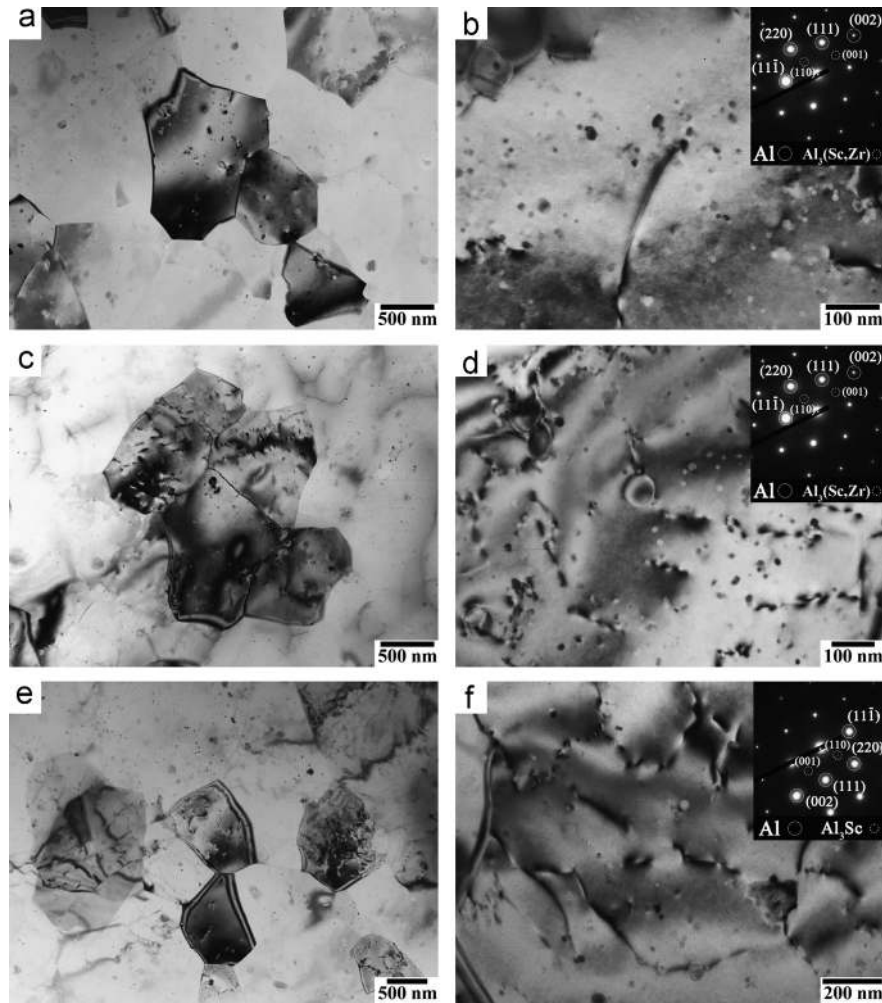
Fig. 6. TEM images of microstructures in the central part of the stir zone in (a, b) the O condition, (c, d) the H323 condition and (e, f) the H18 condition (note the differences in scale): the diffraction patterns in the top right corners of (b), (d) and (f) show the coherent nature of the Al$_3$(Sc,Zr) precipitates (see Section 3.3.1 for details).

Table 2
Microstructural characteristics of stir zone materials.

Material condition	Mean grain diameter (EBSD), μm	Dislocation density (TEM), m^{-2}	HAB fraction (EBSD), %
O+FSW	1.5	2×10^{13}	82
H323+FSW	1.2	4×10^{13}	87
H18+FSW	1.4	5×10^{13}	91

Table 3
Effect of FSW on volume fraction and mean size of Al$_3$(Sc,Zr) dispersoids.

Material condition	Volume fraction, %		Mean diameter, nm	
	Base material	Stir zone	Base material	Stir zone
O	0.1	0.1	9	16
H323	0.1	0.1	9	15
H18	0.1	0.1	9	13

by the rotating pin. In this case, the shear plane normal in the central part of the stir zone would have been parallel to the WD.

The textures were examined by extracting the orientation data from the EBSD maps in Fig. 5, which are presented as 111 and 110 pole figures in Fig. 8. For clarity, the positions of an ideal $B/\bar{B}\{112\}\langle110\rangle$ simple shear texture (which typically develops during FSW of aluminum alloys) are shown as open circles.

It can be seen that the textures were very weak with the peak intensity being only ~1.5 times the value associated with a random state. Moreover, the textures were very ill-defined and could not be unambiguously interpreted in terms of either $B/\bar{B}$ or other simple shear textures.

To assess the effect of the texture on grain-boundary development, misorientation distributions were derived from the textural data and compared with the grain-boundary (real) misorientation distribution in Fig. 9. Whereas the grain-boundary distributions displayed the misorientation data between neighboring pixels in an EBSD map, the texture-derived distributions were obtained by assuming there was no spatial correlation between the pixels. That is, all of the possible misorientations between the sampled pixels (including noncontiguous pixels) were calculated. For comparative purposes, random misorientation distributions were also added to Fig. 9.

It can be seen that the grain-boundary distributions, the texture-derived distributions and the random distributions were generally similar to each other. The nearly random characters of the grain-boundary and texture-derived distributions were presumably related to the very weak texture that evolved in the stir zone (Fig. 8).

3.4. Mechanical properties of welds

3.4.1. Microhardness

Fig. 10 shows the microhardness profiles measured in the O, H323 and H18 conditions (indicated by dotted lines in Fig. 4).
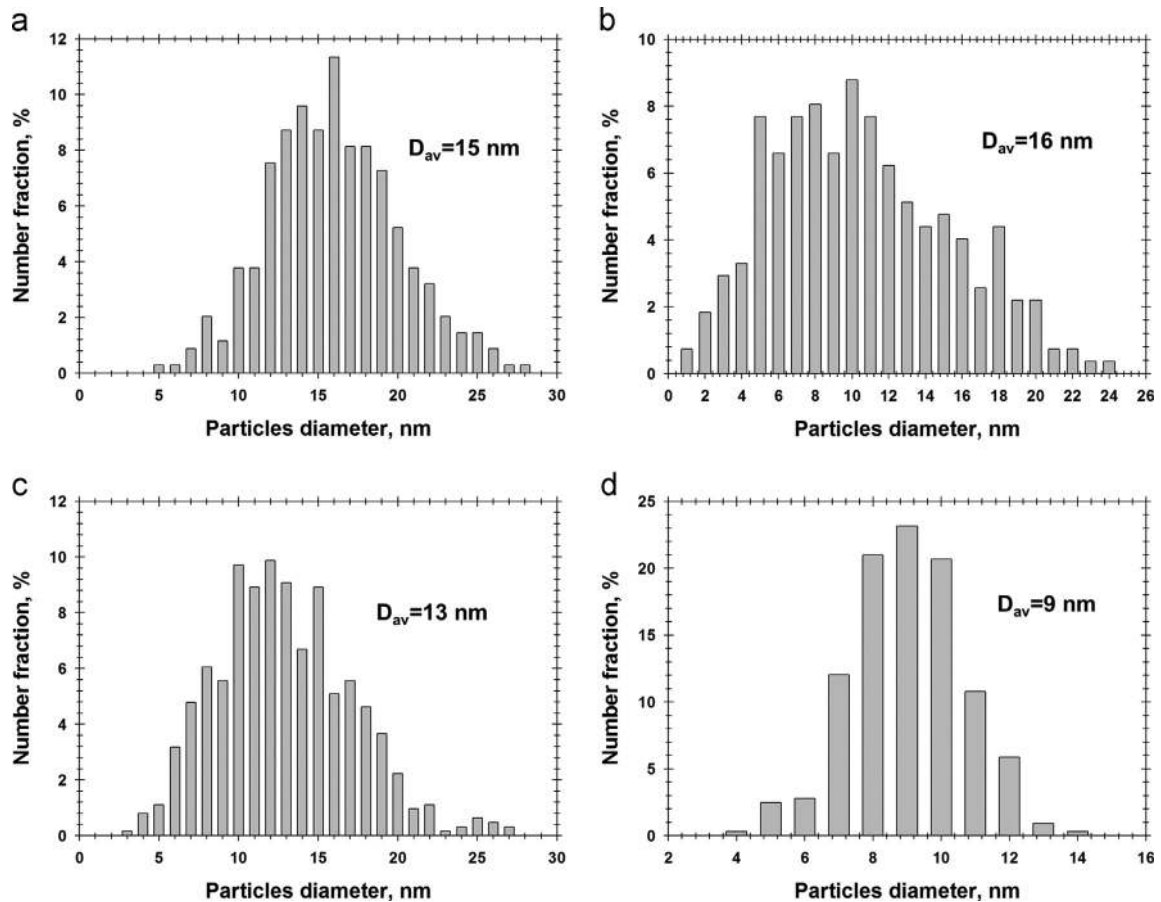
Fig. 7. Size distribution of Al$_3$(Sc,Zr) precipitates measured in the central part of the stir zone in (a) the O condition, (b) the H323 condition and (c) the H18 condition: for comparative purposes, the size distribution of the Al$_3$(Sc,Zr) dispersoids in the base material in the O condition is also given in (d).

The pin and shoulder diameters are also shown in the figure for clarity. To a first approximation, the pin diameter delineates the stir zone, whereas the shoulder diameter indicates the region most affected by heat.

Microhardness traces show no or little variation in hardness between the parent metal and weld for O and H323 conditions, respectively. The H323 material (~120 HV) is slightly harder than the O-condition (~110 HV). There is a significant scattering in the experimental values of microhardness. However, it is apparent that the stir zone may be slightly softer than the H323 condition.

The H18 material has a Vickers microhardness of about 155 HV; this is very high for Al–5% Mg–Sc alloy. The FSW process softens the H18 material with the microhardness reducing by nearly −25% in the stir zone to about 116 HV. Microhardness values on the low plateau in H18 and H323 conditions are the same (Fig. 10). It is worth noting that the value of this softening is significantly less than that in an AA5083H19 alloy [8]. Therefore, Al–Mg–Sc alloys in full hard condition are more resistant to softening under FSW than conventional Al–Mg alloy. In the H18 condition, remarkable softening was observed in the heat-affected zone, and the hardness reducing by nearly −17% to about 116 HV took place in the thermomechanically affected zone (Fig. 10). Microhardness profile for the Al–Mg–Sc alloy in H18 condition is distinctly different from the one in an AA5083H19 alloy [8], in which the low hardness plateau significantly extends out of the shoulder diameter [8]. It is obvious that the nano-scale Al$_3$(Sc,Zr) precipitates in Al–Mg alloys may sustain an extremely work-hardened state in the heat-affected zone and highly reduce softening in the thermomechanically affected zone. The low microhardness

plateau extends from the weld line only to the middle of the thermomechanically affected zone in the fully hardened Al–Mg–Sc alloy (Fig. 10).

3.4.2. Tensile behavior

Fig. 11 shows typical deformation diagrams obtained during transverse and longitudinal tensile tests on the base material, the friction-stir welds and the stir zone material. Duplicate tests showed very similar results; thus, only one set of the diagrams is shown in the figure for each condition. The relevant mechanical properties are summarized in Tables 4–6. Fig. 12 shows the appearance of the friction-stir welds tensioned to failure; the weld zone is outlined in the specimens for clarity.

A significant feature of the deformation diagrams is the repeating oscillations, which indicate the serrated character of the material flow (Fig. 11). In aluminum alloys, this phenomenon is known as the Portevin-Le Chatelier (PLC) effect, which is conventionally attributed to dynamic strain aging [38]. In this study, the magnitude of the oscillations was small relative to the general level of the flow curves (Fig. 11), and therefore this phenomenon was interpreted as type B serrations. These serrations are associated with the irregular movement of the Luders band front. In all of the cases studied, FSW significantly reduced the critical strain for the serrations nearly down to the yield point (Fig. 11).

In the base material, preprocessing from the O to the H323 and H18 conditions had significant strengthening effects (Table 4). In contrast, the stir zone material showed nearly the same strength irrespective of the thermo-mechanical history of the base material
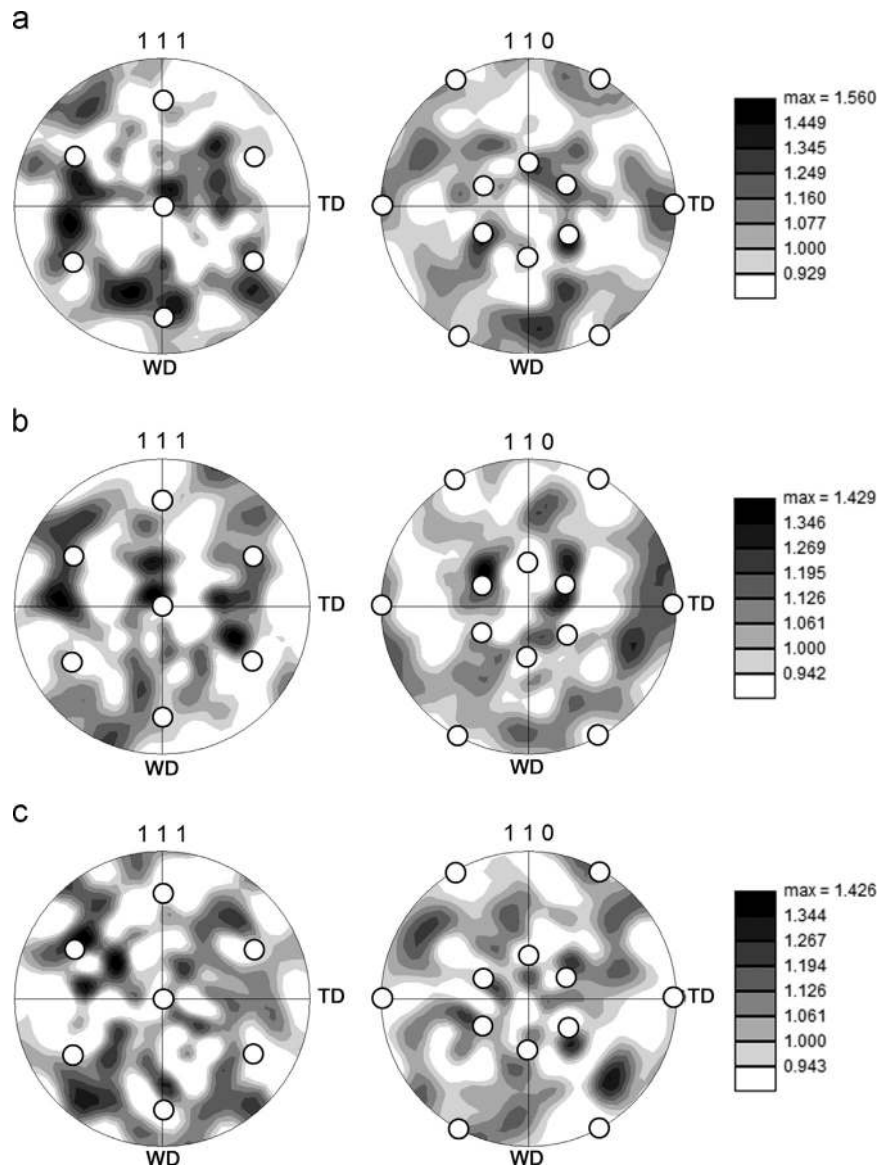
Fig. 8. 111 and 110 pole figures showing the texture in the central part of the stir zone in (a) the O condition, (b) the H323 condition and (c) the H18 condition: for clarity, the positions of the ideal $B/\overline{B}$ {112}⟨110⟩ ideal simple shear orientations are shown as open circles (see Section 3.3.2 for details).

(Table 5). This behavior of the stir zone was obviously associated with nearly the same microstructures and textures that developed in the stir zones of the three welded materials (see Figs. 5–9, Tables 2 and 3). The tensile data generally agreed reasonably well with the microhardness measurements (Fig. 10).

In the O condition, the strength of the stir zone material was somewhat higher than that of the base material (Fig. 11a). In the corresponding friction-stir welds, this difference in strength most likely led to strain initiation and final fracture in the base material region during the transverse tensile tests (Fig. 12). Consequently, the joint efficiency in the O condition was near 100% (Table 6).

In contrast, the stir zone materials in the H323 and H18 conditions were softer than the base material (Fig. 11b and c). This variation in the softness presumably caused strain localization and subsequent fracture in the stir zone area during the transverse tensile tests of the friction-stir welds (Fig. 12). In the H323 state, the difference between the strength of the stir zone and the base material was relatively small (Fig. 11b), and thus the joint efficiency was also near 100% (Table 6). In the H18 condition, this difference was very large (Figs. 10 and 11c), and therefore the respective joint efficiency for the yield strength was only 64% (Table 6).

4. Discussion

4.1. Strengthening mechanisms

As shown in Section 3, FSW drastically changed the grain structure in the stir zone. In the H18 condition, this change in the grain structure significantly affected the joint efficiency, whereas in the O and H323 conditions the effect was very small. Strengthening mechanisms are discussed in this section to elucidate the key issues in the microstructure–strength relationship in Al–Mg–Sc–Zr friction-stir welds.

Assuming that different strengthening mechanisms act independently and thus have additive contributions, the total strength of the Al–Mg–Sc–Zr alloy may be expressed as

$$\sigma = \sigma_0 + \sigma_d + \sigma_p + \sigma_{GB}, \tag{1}$$

where σ_0 denotes the threshold strength, σ_d denotes the dislocation strengthening, σ_p denotes the precipitation strengthening and σ_{GB} denotes the grain-boundary strengthening.

In Al–Mg alloys, the threshold strength is believed to be dominated by solid solution strengthening, which is controlled
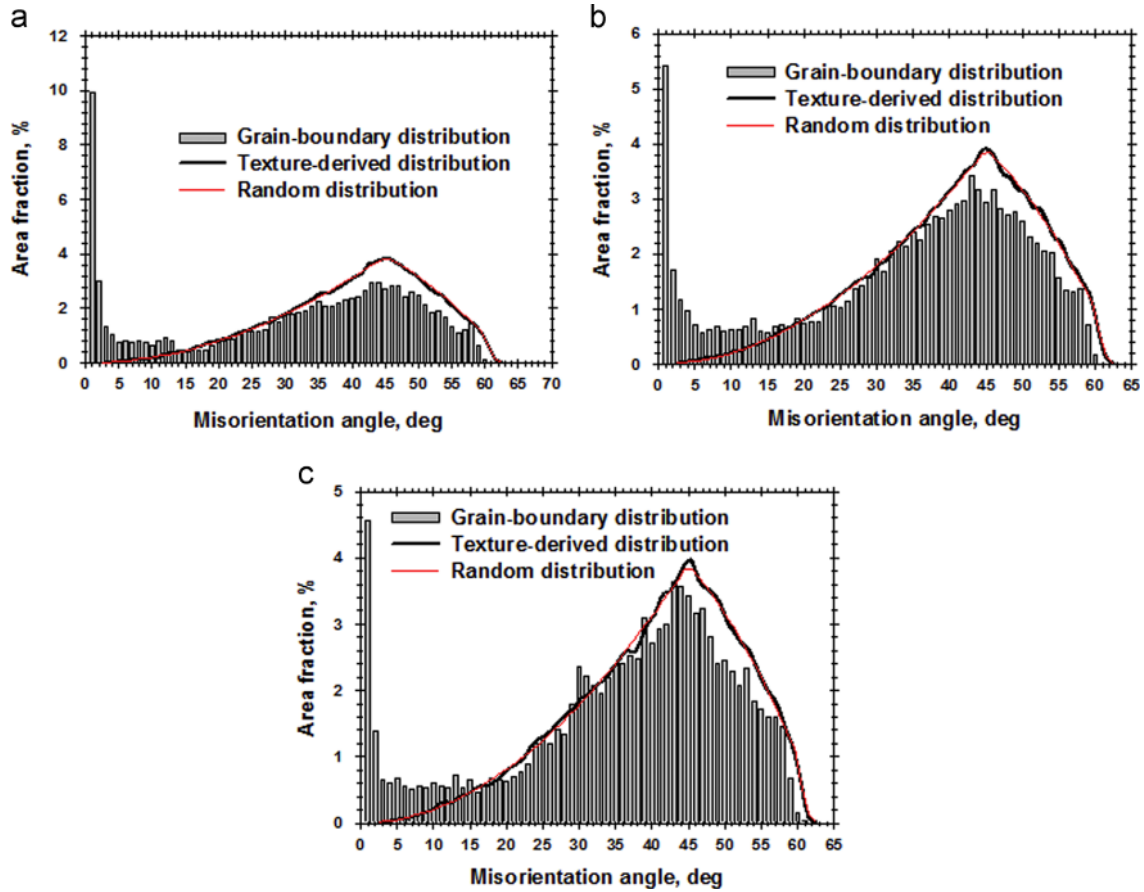
Fig. 9. Misorientation-angle distributions in the central parts of the stir zone in (a) the O condition, (b) the H323 condition and (c) the H18 condition (see Section 3.3.2 for details).
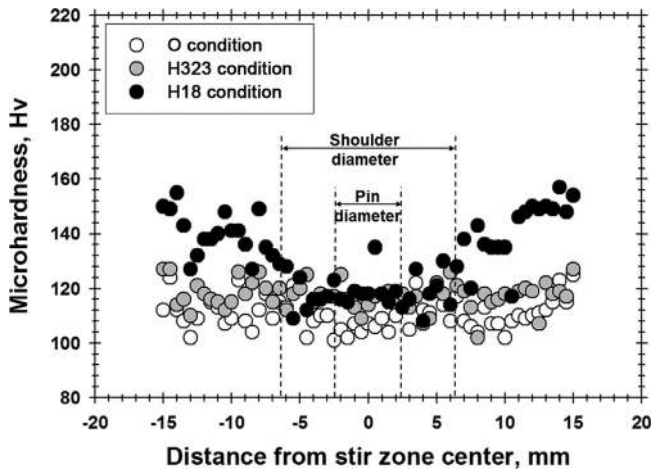

Fig. 10. Microhardness profiles measured across transversal cross-section of friction-stir welds produced in O, H323 and H18 conditions (indicated by dotted lines in Fig. 4).

by the magnesium solute content. In the material used in this study (5 wt% magnesium), the solid solution strengthening at ambient temperature is estimated to be approximately 100 MPa [20]. In this study, no evidence was found for the precipitation or dissolution of second-phase particles during material preprocessing or FSW. Therefore, the threshold strength was considered to be unchanged in all of the conditions studied.

The dislocation strengthening is usually described as

$$\sigma_d = M\alpha Gb\rho^{0.5}, \tag{2}$$

where M is the Taylor factor, α is a number often valued at 0.24, G denotes the shear modulus of aluminum (25,400 MPa), b denotes the Burgers vector (0.286 nm), and ρ denotes the dislocation density.

The mean Taylor factor was derived from the EBSD data assuming uniaxial tension on the WD. This factor was found to vary from 3.02 to 3.14 depending on the particular condition. The calculated dislocation strengthening is shown in Table 7.

4.2. Precipitation strengthening

In Al–Mg–Sc alloys, precipitation strengthening may be associated with particle shearing or with particle bowing mechanisms. Kendig et al. showed that the first mechanism predominates for dispersoid sizes below ∼25 nm, whereas the second mechanism is favored for coarser particles [20]. In this work, the precipitates were typically finer than 25 nm in diameter (Fig. 6): therefore, the particle cutting mechanism should have prevailed.

In this case, the strengthening effect is believed to have resulted primarily from the formation of an anti-phase boundary (APB) within the sheared particle, mainly. The strengthening may be estimated using the following equation [20]:

$$\sigma_p = M\frac{\gamma^{1.5}}{b^2}\left(\frac{rf}{G}\right)^{0.5}, \tag{3}$$

where γ denotes the energy required to form the APB, r denotes the radius of the particles being cut and f denotes the particle volume fraction.
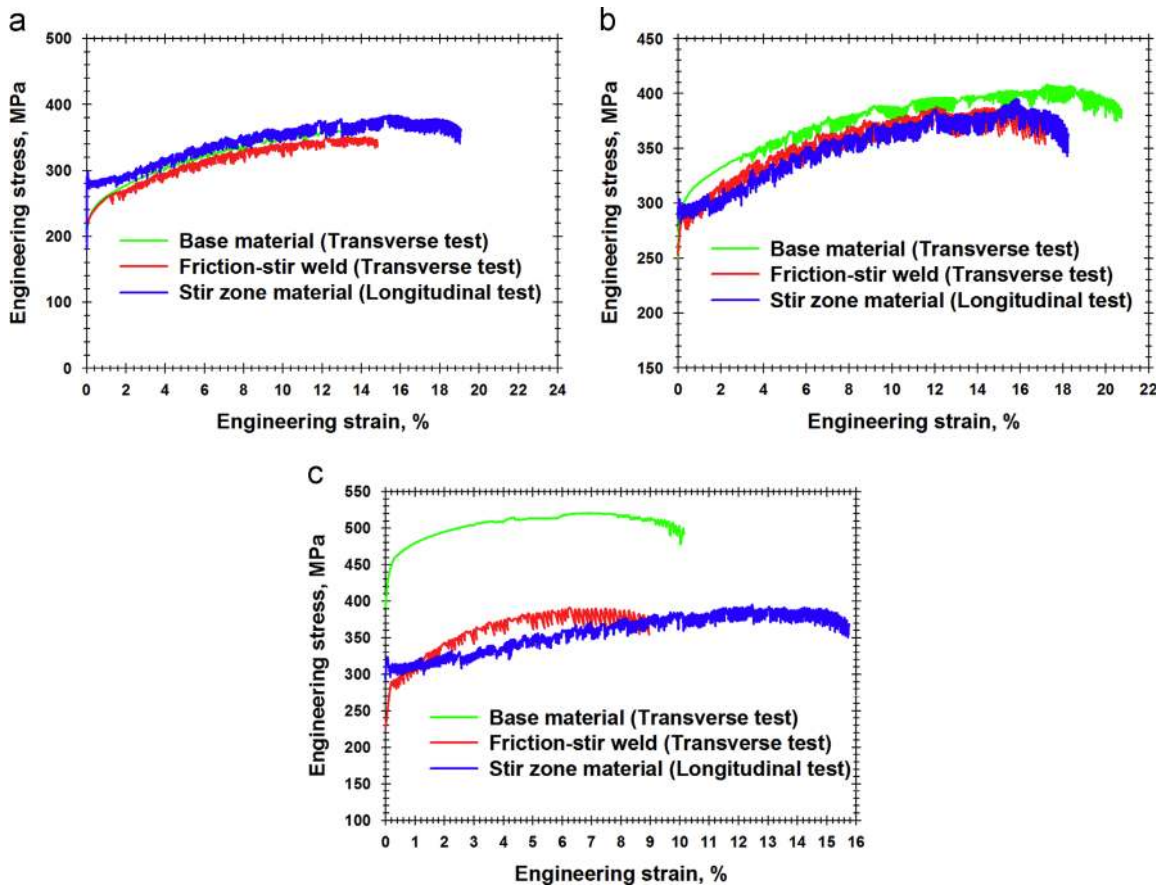
Fig. 11. Typical deformation diagrams of the base material, the friction-stir welds and the stir zone material in (a) the O condition, (b) the H323 condition (c) and the H18 condition.

Table 4
Mechanical properties of base materials.

Material condition	Tensile properties in ED (RD)/TD		
	Yield strength, MPa	Ultimate tensile strength, MPa	Ductility, %
O	278/232	418/359	23/14
H323	307/300	419/404	17/17
H18	463/447	514/519	5/9

Table 5
Mechanical properties of stir zone materials tensioned in the WD.

Material condition	Yield strength, MPa	Ultimate tensile strength, MPa	Ductility, %
O	275	385	19
H323	275	380	15
H18	305	395	16

Table 6
Mechanical properties of friction-stir welds tensioned in the TD.

Material condition	Tensile properties of friction-stir welds			Joint efficiency, %			Failure location
	YS, MPa	UTS, MPa	δ, %	YS	UTS	δ	
O	222	352	17	96	98	100	Base material
H323	283	382	17	94	95	100	Stir zone
H18	288	385	9	64	74	100	Stir zone
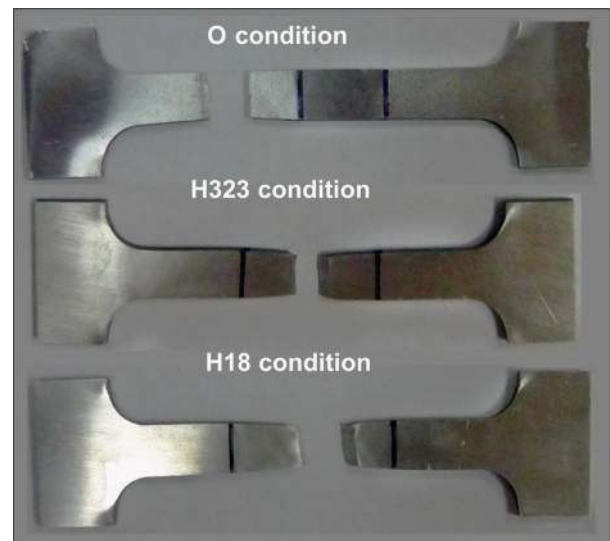
Fig. 12. Appearance of friction-stir welded transverse specimens tensioned to failure. The black lines indicate the weld borderlines.

It is difficult to determine the APB energy accurately. The APB energy has been reported to vary from 0.1 to 0.67 J/m² depending on the calculation method used [20]. In this work, an APB energy of 0.185 J/m² (as recommended by Kendig et al. [20]) was considered to be a reasonable value. The calculated precipitation strengthening is shown in Table 7.

Table 7
Contribution of strengthening mechanisms.

Condition	Predicted strengthening, MPa					Measured yield strength, MPa
	Solid-solution	Dislocation	Precipitation	Grain-boundary	Total	
Base material						
O	100	17	39	95	251	278
H323	100	35	41	153	329	307
H18	100	154	41	286	581	463
Stir zone						
O+FSW	100	24	53	132	309	300
H323+FSW	100	34	51	150	335	305
H18+FSW	100	38	47	132	317	325

4.3. Grain-boundary strengthening

Grain-boundary strengthening is conventionally described in terms of the well-known Hall–Petch relationship:

$$\sigma_{GB} = k_{HP} d_G^{-0.5}, \qquad (4)$$

where k_{HP} is the Hall–Petch constant and d_G denotes the mean grain size.

In Al–Mg alloys, the Hall–Petch constant has been reported to vary from 0.15 to 0.26 MPa m$^{0.5}$ [38,39]; in this work, the Hall–Petch constant was taken to be 0.17 MPa m$^{0.5}$, as recommended by Kendig et al. [20].

The YS vs. grain size dependencies obey the Hall–Petch relation well for completely recrystallized microstructures similar to those that developed in the stir zone (Figs. 5 and 6). The grain-boundary strengthening calculated for these three materials is given in Table 7. On the other hand, all three states of the base materials exhibited well-defined substructures (Figs. 2 and 3), which should affect significantly the dislocation motion. Thus, the classical form of the Hall–Petch equation should not have been applicable in the present cases.

The EBSD measurements showed that the LAB fraction for these conditions ranged from 68% to 82% (Table 1). It therefore may be concluded that LABs contributed considerably to grain-boundary strengthening in these materials.

In contrast to HABs, low-angle (i.e., dislocation) boundaries are assumed to be penetrable to slip and can contribute to strengthening via forest hardening. The strengthening effect of the LABs may therefore be given by [40]

$$\sigma_{GB} = \left(M\alpha G \sqrt{3b\theta_{LAB}} \right) d_{SG}^{-0.5}, \qquad (5)$$

where θ_{LAB} denotes the mean LAB misorientation and d_{SG} denotes the mean subgrain size.

In the base materials, the subgrains seen in EBSD maps (Fig. 1) were typically considerably coarser than those observed by TEM (Fig. 3). This result may indicate that most of the LABs had misorientations below 2° and thus could not be reliably detected by EBSD. That is, the EBSD data could not be used to calculate the θ_{LAB} parameter.

There is a large scatter in the measurements in the scientific literature of the mean LAB misorientation in heavily deformed aluminum. This scatter can be partly attributed to the co-existence of two different types of LABs (i.e., incidental dislocation boundaries and boundaries that are geometrically necessary) that accumulate misorientation with different speeds. Nevertheless, a magnitude of 2–3° is often reported as a reasonable mean misorientation, e.g., [34,41]. In this work, a mean LAB misorientation of 3° was used. The calculated LAB strengthening is shown in Table 7.

4.4. Strength of friction-stir welds

Table 7 summarizes the contributions of different strengthening mechanisms to the final strength of the materials in the preprocessed and friction-stir welded states. With the exception of the preprocessed H18 condition, the difference between the predicted and measured strengths was relatively low and does not exceed 10%. Taking into account the uncertainty in many of the parameters used in the calculations (particularly, the threshold value of the θ_{LAB}), this accuracy was good. The relatively large error in the preprocessed H18 state is considered to be related to an overestimate of the mean LAB misorientation.

Surprisingly, the precipitation strengthening in the stir zone was predicted to *increase*. This prediction was related to the subtle coarsening of dispersoids (Table 3) and the respective enlargement of the particle cutting stresses. However, this effect was rather small (Table 7) and was unlikely to affect significantly the material strength.

The most striking result was the relatively low strengthening promoted by the formation of the fine-grained structure in the stir zone (Table 7). In the work-hardened H323 and H18 conditions, the grain-boundary strengthening associated with HABs in the stir zone was comparable or even weaker that the LAB strengthening in the preprocessed state (Table 7); this effect is thought to be related to the relatively small subgrain size in these base materials (Table 1). Thus, FSW did not significantly change the material strength in the O and H323 conditions (Fig. 10), and therefore these welds exhibited a joint efficiency close to 100% (Table 6). In other words, almost full strength welds can be obtained in Al–Mg–Sc alloys in partially hardened and stabilized condition.

Material softening in the stir zone was predicted in the H18 condition (Table 7). This phenomenon was primarily attributed to the elimination of the dislocation hardening as well as LAB strengthening in the base material (Table 7) due to the occurrence of dynamic and/or post-dynamic recrystallization [3,8,42] during FSW. Consequently, the joint efficiency in the H18 condition was relatively low (Table 6). If recrystallization process is an inevitable consequence of FSW of aluminum alloys, full strength welds cannot be obtained in Al–Mg–Sc alloys in fully hardened condition.

It is worth noting, however, that fully hardened materials are rarely used in practice because of their relatively high susceptibility to stress-corrosion cracking [1,2]. To avoid this undesirable effect, these materials are usually subjected to stabilizing (i.e., recovery) annealing. The present study shows that the joint efficiency in this condition should be high. Thus, it is expected

that FSW can produce high-strength joints for *commercially useful* work-hardened products from Al–Mg–Sc–Zr alloys.

5. Conclusions

In this study, the microstructure and mechanical properties of a friction-stir-welded Al–5.4Mg–0.2Sc–0.1Zr alloy were investigated, and particular emphasis was paid to structure–property relationships. The main conclusions from this work are given below.

(1) FSW was demonstrated to be feasible for producing defect-free welds in the annealed (O) condition, the quarter-hardened and stabilized (H323) condition and the fully hardened (H18) condition. The joint efficiency for the yield strength in the O and H323 conditions was determined to be nearly 100%. In the fully hardened H18 condition, significant material softening was found in the stir zone, resulting in a joint efficiency of only 64%.

(2) In all cases, FSW produced a fully recrystallized structure with micron-scale grains in the stir zone. Nano-scale $Al_3(Sc,Zr)$ dispersoids were found to coarsen in the stir zone from 9 to $\sim$15 nm but retained their coherency with the matrix.

The model describing the strength of the friction-stir welds was proposed. According to this model, the high joint efficiency in the O and H323 conditions was related to the preservation of the coherent nano-scale dispersoids as well as with extensive grain refinement. On the other hand, substantial material softening in the H18 state was attributed to the elimination of the work hardening effect due to recrystallization occurring during FSW.

Acknowledgments

References

[1] I.J. Polmear, Light Alloys: From Traditional Alloys to Nanocrystals, 4th ed., Butterworth-Heinemann/Elsevier, UK, 2006.
[2] E.A. Brandes, G.B. Brook (Eds.), Smithells Light Metals Handbook, Butterworth-Heinemann, 1998.
[3] P.L. Threadgill, A.J. Leonard, H.R. Shercliff, P.J. Withers, Int. Mater. Rev. 54 (2009) 49–93.
[4] R.S. Mishra, Z.Y. Ma, Mater. Sci. Eng. R 50 (2005) 1–78.
[5] R. Nandan, T. DebRoy, H.K.D.H. Bhadeshia, Prog. Mater. Sci. 53 (2008) 980–1023.
[6] R.W. Fonda, P.S. Pao, H.N. Jones, C.R. Feng, B.J. Connolly, A.J. Davenport, Mater. Sci. Eng. A 519 (2009) 1–8.
[7] M.M. Attallah, C.L. Davis, M. Strangwood, Sci. Technol. Weld. Join. 12 (2007) 361–369.
[8] M. Peel, A. Steuwer, M. Preuss, P.J. Withers, Acta Mater. 51 (2003) 4791–4801.
[9] H.L. Hao, D.R. Ni, H. Huang, D. Wang, B.L. Xiao, Z.R. Nie, Z.Y. Ma, Mater. Sci. Eng. A 559 (2013) 889–896.
[10] R. Kapoor, N. Kumar, R.S. Mishra, C.S. Huskamp, K.K. Sankaran, Mater. Sci. Eng. A 527 (2010) 5246–5254.
[11] A. Cobello Munoz, G. Ruckert, B. Huneau, X. Sauvage, S. Marya, J. Mater. Process. Technol. 197 (2008) 337–343.
[12] X. Sauvage, A. Dede, A. Cabello Munoz, B. Huneau, Mater. Sci. Eng. A 491 (2008) 346–371.
[13] Y.S. Sato, H. Kokawa, M. Enomoto, S. Jogan, T. Hashimoto, Met. Mater. Trans. 30A (1999) 3125–3130.
[14] J. Røyset, N. Ryum, Int. Mater. Rev. 50 (2005) 19–44.
[15] T.G. Nieh, L.M. Hsiung, J. Wadsworth, R. Kaibyshev, Acta Mater. 46 (1998) 2789–2800.
[16] O. Sitdikov, T. Sakai, E. Avtokratova, R. Kaibyshev, K. Tsuzaki, Y. Watanabe, Acta Mater. 56 (2008) 821–834.
[17] R. Kaibyshev, A. Mogucheva, A. Dubyna, Mater. Sci. Forum 55 (2012) 706–709.
[18] Yu.A. Filatov, V.I. Yelagin, V.V. Zakharov, Mater. Sci. Eng. A 280 (2000) 97–101.
[19] M.E. Van Dalen, D.N. Seidman, D.C. Dunand, Acta Mater. 56 (2008) 4369–4377.
[20] K.L. Kendig, D.B. Miracle, Acta Mater. 50 (2002) 4165–4175.
[21] C.B. Fuller, J.L. Murray, D.N. Seidman, Acta Mater. 53 (2005) 5401–5413.
[22] J. Zhao, F. Jiang, H. Jian, K. Wen, L. Jiang, X. Chen, Mater. Des. 31 (2010) 306–311.
[23] H. Zhen-bo, P. Yong-yi, Y. Zhi-min, L. Xue-feng, Trans. Nonferrous Met. Soc. China 21 (2011) 1685–1691.
[24] Y.S. Sato, M. Urata, H. Kokawa, Metall. Mater. Trans. A 33 (2002) 625–635.
[25] E.A. Marquis, D.N. Seidman, Acta Mater. 53 (2005) 4259–4268.
[26] C.B. Fuller, D.N. Seidman, Acta Mater. 53 (2005) 5415–5428.
[27] A. Deschamps, L. Lae, P. Guyot, Acta Mater. 55 (2007) 2775–2783.
[28] A. Tolley, V. Radmilovic, U. Dahmen, Scr. Mater. 52 (2005) 621–625.
[29] N.Q. Vo, D.C. Dunand, D.N. Seidman, Acta Mater. 60 (2012) 7078–7089.
[30] F.J. Humphreys, J. Microsc. 195 (1999) 170–185.
[31] R. Kaibyshev, K. Shipilova, F. Musin, Y. Motohashi, Mater. Sci. Eng. A 396 (2005) 341–351.
[32] F.J. Humphreys, M. Hatherly, Recrystallization and Related Annealing Phenomena, Elsevier, Oxford, 2005.
[33] D.A. Hughes, N. Hansen, High angle boundaries formed by grain subdivision mechanisms, Acta Mater. 45 (1997) 3871–3886.
[34] P.J. Hurley, F.J. Humphreys, Acta Mater. 51 (2003) 1087–1102.
[35] N. Kumar, R.S. Mishra, C.S. Huskamp, K.K. Sankaran, Scr. Mater. 64 (2011) 576–579.
[36] R.W. Fonda, K.E. Knipling, J.F. Bingert, Scr. Mater. 58 (2007) 343–348.
[37] R.W. Fonda, K.E. Knipling, Sci. Tech. Weld. Join. 16 (2011) 288–294.
[38] B.Q. Han, Z. Lee, S.R. Nutt, E.J. Lavernia, F.A. Mohamed, Metall. Mater. Trans. A 34 (2003) 603–613.
[39] V.L. Tellkamp, A. Melmed, E.J. Lavernia, Metall. Mater. Trans. A 32 (2001) 2335–2343.
[40] N. Hansen, Scr. Mater. 51 (2004) 801–806.
[41] Q. Liu, X. Huang, D.J. Lloyd, N. Hansen, Acta Mater. 50 (2002) 3789–3802.
[42] T. Sakai, A. Belyakov, R. Kaibyshev, H. Miura, J.J. Jonas, Prog. Mater. Sci. 60 (2014) 130–207.